



Rational solvent molecule tuning for high-performance lithium metal battery electrolytes

Zhiao Yu^{1,2}, Paul E. Rudnicki¹, Zewen Zhang³, Zhuojun Huang³, Hasan Celik⁴, Solomon T. Oyakhire¹, Yuelang Chen^{1,2}, Xian Kong¹, Sang Cheol Kim³, Xin Xiao³, Hansen Wang³, Yu Zheng^{1,2}, Gaurav A. Kamat⁵, Mun Sek Kim^{1,3}, Stacey F. Bent¹, Jian Qin¹, Yi Cui^{3,5} and Zhenan Bao¹

Electrolyte engineering improved cycling of Li metal batteries and anode-free cells at low current densities; however, high-rate capability and tuning of ionic conduction in electrolytes are desirable yet less-studied. Here, we design and synthesize a family of fluorinated-1,2-diethoxyethanes as electrolyte solvents. The position and amount of F atoms functionalized on 1,2-diethoxyethane were found to greatly affect electrolyte performance. Partially fluorinated, locally polar $-\text{CHF}_2$ is identified as the optimal group rather than fully fluorinated $-\text{CF}_3$ in common designs. Paired with 1.2 M lithium bis(fluorosulfonyl)imide, these developed single-salt-single-solvent electrolytes simultaneously enable high conductivity, low and stable overpotential, >99.5% Li|Cu half-cell efficiency (up to 99.9%, $\pm 0.1\%$ fluctuation) and fast activation (Li efficiency >99.3% within two cycles). Combined with high-voltage stability, these electrolytes achieve roughly 270 cycles in 50- μm -thin Li|high-loading-NMC811 full batteries and >140 cycles in fast-cycling Cu|microparticle-LiFePO₄ industrial pouch cells under realistic testing conditions. The correlation of Li⁺-solvent coordination, solvation environments and battery performance is investigated to understand structure-property relationships.

Lithium (Li) metal battery is highly pursued as the next-generation power source^{1,2}. However, the implementation of Li metal anode is hindered by poor cycle life, which originates from uncontrollable Li/electrolyte side reactions and the resulting unstable and fragile solid–electrolyte interphase (SEI). Subsequently, the notorious issues such as cracking of SEI, dendritic Li growth and ‘dead Li’ formation generate a vicious cycle, leading to irreversible Li consumption and finally battery failure^{3–5}.

Liquid electrolyte engineering is regarded as a cost-effective and pragmatic approach^{6–10} to address the root cause, that is, uncontrollable parasitic reactions between Li metal anodes and electrolytes. By fine-tuning electrolyte components, the SEI chemistry and Li morphology can be regulated to improve Li metal cyclability. Several promising strategies have been investigated, including high concentration electrolytes¹¹, localized high concentration electrolytes^{12,13}, mixed solvents^{14–16}, additive tuning¹⁷, liquified gas electrolytes¹⁸, dual-salt-dual-solvent electrolytes^{19,20} and single-salt-single-solvent electrolytes^{21–25}.

To enable practical Li metal or anode-free batteries, several key requirements^{10,21,26} should be simultaneously fulfilled for a promising electrolyte. First, high Coulombic efficiency (CE) including the initial cycles, that is, fast activation of Li metal anode; second, anodic stability to avoid cathode corrosion; third, low electrolyte consumption under practical operating conditions such as lean electrolyte and limited Li inventory; fourth, moderate Li salt concentration for cost-effectiveness and last, high boiling point and the absence of any gassing issue to ensure processability and safety.

Beyond these requirements, high ionic conductivity is another critical parameter for realistic cycling rates. Several papers^{21,27–29}

reported improved Li metal stability using weakly solvating solvents. However, insufficient solvation will cause ion clustering, poor ion motion and low solubility of salts, leading to low ionic conductivity. Therefore, fine-tuning of the solvation capability³⁰ of the solvent is necessary to simultaneously achieve Li metal cyclability, oxidative stability and ionic conductivity of the electrolyte.

In this work, we systematically investigate a family of fluorinated-1,2-diethoxyethane (fluorinated-DEE) molecules that are readily synthesized on large scales to use as the electrolyte solvents. Selected positions on 1,2-diethoxyethane (DEE, distinct from the diethyl ether previously reported²⁴) are functionalized with various numbers of fluorine (F) atoms through iterative tuning, to reach a balance between CE, oxidative stability and ionic conduction (Fig. 1a). Paired with 1.2 M lithium bis(fluorosulfonyl)imide (LiFSI), these fluorinated-DEE-based, single-salt-single-solvent electrolytes are thoroughly characterized. Their Li⁺-solvent binding energies and geometries (from density functional theory (DFT) calculations), solvation environments (from solvation free energy measurements³¹, ⁷Li-nuclear magnetic resonance (NMR), molecular dynamics simulations and diffusion-ordered spectroscopy (DOSY)³²), and results in batteries (measured ion conductivities and cell overpotentials) are found to be tightly correlated with each other. The above studies lead to an unexpected finding: a partially fluorinated, locally polar $-\text{CHF}_2$ group results in higher ionic conduction than fully fluorinated $-\text{CF}_3$ while still maintaining excellent electrode stability. Specifically, the best-performing F4DEE and F5DEE solvents both contain $-\text{CHF}_2$ group(s). In addition to high ionic conductivity and low and stable overpotential, they achieve roughly 99.9% Li CE with $\pm 0.1\%$ fluctuation as

¹Department of Chemical Engineering, Stanford University, Stanford, CA, USA. ²Department of Chemistry, Stanford University, Stanford, CA, USA.

³Department of Materials Science and Engineering, Stanford University, Stanford, CA, USA. ⁴College of Chemistry Nuclear Magnetic Resonance Facility (CoC-NMR), University of California, Berkeley, CA, USA. ⁵Stanford Institute for Materials and Energy Sciences, SLAC National Accelerator Laboratory, Menlo Park, CA, USA. ✉e-mail: jianq@stanford.edu; yicui@stanford.edu; zbao@stanford.edu

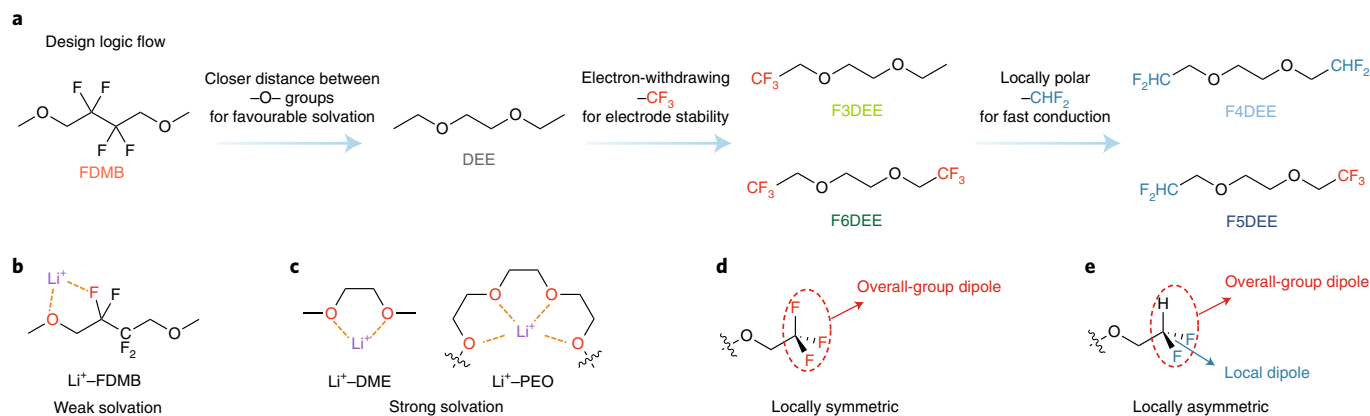


Fig. 1 | Step-by-step design principles of the fluorinated-DEE solvent family. **a**, Logical flow, starting from FDMB, for the design of the fluorinated-DEE family. **b**, Weak Li^+ -FDMB coordination structure. **c**, Conventional strong coordination structure of Li^+ -EO segments. Two examples are given here: Li^+ -DME in liquid electrolytes and Li^+ -polyethylene oxide (PEO) in solid polymer electrolytes. **d,e**, Spatial configuration and dipole direction of $-\text{CF}_3$ (**d**) and $-\text{CHF}_2$ (**e**).

well as fast activation, that is, the CEs of the Li||copper (Cu) half cells reach >99.3% from the second cycle. Aluminium (Al) corrosion is also suppressed due to the oxidative stability that originates from suitable amount of fluorination. These features enable roughly 270 cycles in thin Li (50- μm thick)||high-loading-NMC811 ($\text{LiNi}_{0.8}\text{Mn}_{0.1}\text{Co}_{0.1}\text{O}_2$, roughly 4.9 mAh cm^{-2}) full batteries and >140 cycles in fast-cycling anode-free Cu||microparticle-LFP (LiFePO_4 , roughly 2.1 mAh cm^{-2}) industrial pouch cells, both of which stand among the state-of-the-art performances.

Design logic of fluorinated-DEE molecular family

Despite the high stability towards Li metal anodes and high-voltage cathodes, our previously reported fluorinated 1,4-dimethoxybutane (FDMB) solvent (Fig. 1a) was found to have the drawbacks of poor ionic conductivity and large overpotential^{16,21,33}, which stem from the weak solvation ability of FDMB molecules (Fig. 1b). Such a feature hindered ion diffusion due to the formation of ionic clusters as most electrolyte solvates, while on the other hand benefiting Li metal anode stability^{11,34}. To address this issue, we rationalize that ethylene oxide structure may be desirable as it is a known and widely used segment^{27,35} for good solvation and separating Li^+ and the anion. The ether groups in the ethylene oxide segment, separated by two methylene groups, can form a stable five-member ring with Li^+ (Fig. 1c), thus enhancing cation-anion separation. Such a chelating structure has been commonly observed in liquid electrolytes²⁷ containing 1,2-dimethoxyethane (DME) and in solid polymer electrolytes³⁵ using polyethylene oxide. However, here we select DEE (Fig. 1a) instead of DME as the starting backbone for the following additional reasons. First, the DEE electrolyte has been inadequately studied in the community despite recent reports on its superior high-rate performance than DME for Li metal^{27,28} and silicon³⁶ anodes. Second, the ethyl terminal groups of DEE provide more structural tunability than DME and suitable β -fluorination^{32,37,38} is expected to endow DEE with both stability and high conductivity.

As will be elaborated in the following sections, the Li metal CE and oxidative stability of unmodified DEE still fall short when tested under strict full-cell conditions, albeit performing slightly better than DME. Therefore, starting from DEE structure, we first incorporate the electron-withdrawing $-\text{CF}_3$ groups³⁹ in the β -position of DEE, to enhance both Li metal and oxidative stability while retaining its solvation ability of $-\text{O}-$ groups (Fig. 1a,d). The two obtained electrolyte solvents, F3DEE and F6DEE (Fig. 1a), are found to outperform their DEE counterpart in Li metal batteries, although overfluorination decreases the ionic conductivity of

F6DEE. Next, we further finely tune the degree of fluorination, that is, changing from $-\text{CF}_3$ groups to $-\text{CHF}_2$, to obtain more ionically conductive and stable solvents, F4DEE and F5DEE (Fig. 1a). The partially fluorinated, asymmetric $-\text{CHF}_2$ group, as will be discussed in detail later, contains a local dipole (Fig. 1e) that enables strong intermolecular interactions in F4DEE and F5DEE and better Li^+ solvation than its all-fluorinated, symmetric counterpart, $-\text{CF}_3$ (Fig. 1d). The stronger intermolecular interaction is also evidenced by the high boiling points and viscosities measured for F4DEE and F5DEE (Supplementary Figs. 1 and 2 and Supplementary Table 1). The iteratively designed molecules F4DEE and F5DEE integrate several desired properties, including fast ion conduction, low and stable cell overpotential, high Li metal efficiency, fast activation and oxidative stability.

None of the designed molecules are commercially available, and they were obtained by two-step syntheses on large scales (Methods). The general physicochemical properties of this molecular family and their 1.2M LiFSI electrolytes are determined and shown in Supplementary Table 1.

Improved ionic transport by experimental results

The critical targets in this work are to improve the ionic conductivity and interfacial transport issues of the already high-performing FDMB electrolyte. The 1M LiFSI/FDMB electrolyte was used to maintain consistency with our previous reports^{16,21,33} while 1.2M LiFSI was dissolved in fluorinated-DEEs for optimized conductivity. The ionic conductivities measured with separators followed the trend of $\text{LP40} \cong \text{DEE} \gg \text{F4DEE} \cong \text{F3DEE} > \text{F5DEE} \gg \text{F6DEE} \cong \text{FDMB}$ (Fig. 2a), which is fully consistent with our rationales. Those measured without separators by Swagelok cells showed a similar trend (Fig. 2b, Supplementary Fig. 2 and Supplementary Table 1), although the values are higher due to the absence of the separator.

Li||Li symmetric cells were used to evaluate the overall ionic transport, especially interfacial conduction. As shown in Fig. 2c, the overpotential of 1M LiFSI/FDMB cell vastly increased with cycling; by contrast, the cells using fluorinated-DEE electrolytes maintained stable and low overpotentials. The electrochemical impedance spectra (EIS) of Li||Li cells and the voltage plateau of Li||Cu cells at different cycle numbers confirmed these cycling observations (Supplementary Figs. 3–9). Although the large overpotential increase in the FDMB electrolyte caused only a small capacity drop in full cells according to our previous reports^{16,21,33}, the excellent maintenance of low overpotential in fluorinated-DEE electrolytes is required for realistic batteries. The zoomed-in plot of Li||Li cycling

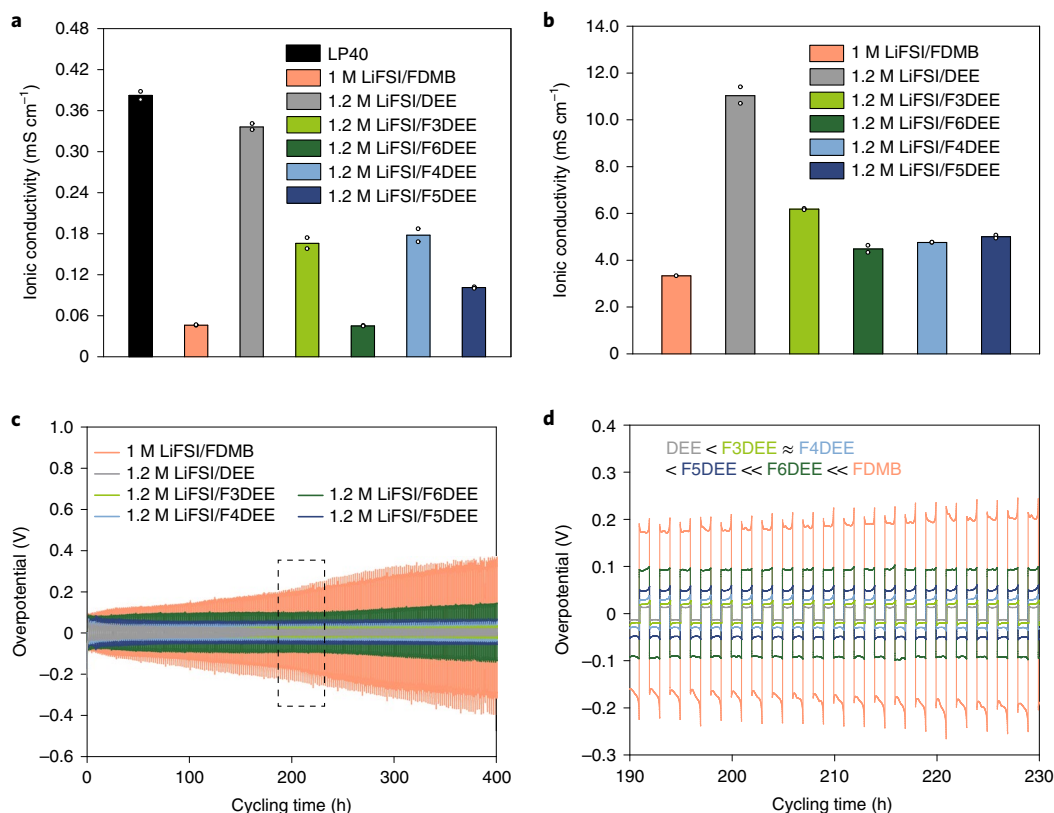


Fig. 2 | Ionic conductivity and cycling overpotential of FDMB and fluorinated-DEE electrolytes. a, b, Ionic conductivities of developed electrolytes with (a) and without (b) separators. Each bar stands for the mean of two replicated ion conductivity measurements and every single measurement is shown with hollow dots. The 1 M LiFSI/FDMB data in b were extracted from ref. ²¹. **c, d,** Cycling performance of Li||Li symmetric cells. Note: d is a portion of c (from 190 h to 230 h) to enable visualization of the overpotential trends.

overpotentials shows the trend of DEE < F3DEE \approx F4DEE < F5DEE \ll F6DEE \ll FDMB (Fig. 2d), which is in accord with the inverse of the ion conductivity trends mentioned above.

Rationales for improved ionic conduction

In addition to the experimental observations, we here rationalize the improvement of ionic transport in fluorinated-DEE electrolytes via thorough theoretical studies, and correlate both theoretical and experimental results for better understanding the structure–property relationships.

We first used DFT to determine optimized binding configurations between Li⁺ and each type of solvent molecule (Fig. 3a–f). While the coordination structure of Li⁺–FDMB and Li⁺–DEE matched with those in the previous report²¹, the Li⁺ ions all showed tripod or tetrapod coordination geometry with fluorinated-DEEs whose F atoms interacted with Li⁺ ions. The Li⁺ showed stronger interaction (that is, shorter Li–F distance) with –CHF₂ than –CF₃. Taking Li⁺–F5DEE as a representative example (Fig. 3f), the Li–F (on –CHF₂) distance was 1.96 Å versus 2.04 Å for –CF₃. The nonparticipation of –CF₃ in Li⁺ solvation was also proved by Amanchukwu et al.²⁵ recently. Such a stronger interaction between Li⁺ and the –CHF₂ group can be rationalized by the fact that –CHF₂ group is locally polar and more negatively charged than –CF₃ in the calculated electrostatic potentials (Fig. 1e and Supplementary Fig. 10). The upfield shift of –CHF₂ signals detected by ¹⁹F-NMR spectra of fluorinated-DEE electrolytes also supports this Li–F interaction^{40,41} (Supplementary Fig. 11).

Molecular dynamics simulations were conducted to further investigate the Li⁺ solvation sheath and determine the distribution of Li⁺ solvates (Fig. 3g–l and Supplementary Figs. 12–17).

The functional groups tightly interacting with Li⁺ in the first solvation sheath were consistent with those in the aforementioned DFT results. Particularly, the Li–F radial distribution functions (RDFs) of simulated 1.2 M LiFSI/F5DEE clearly demonstrated more F atoms on –CHF₂ participating in Li⁺ solvation than those on –CF₃ (Supplementary Fig. 17). More information was provided by the distribution of Li⁺ solvates, that is, percentages of solvent surrounded Li⁺ (SSL), Li⁺–anion single pair (LASP) and Li⁺–anion cluster (LAC), each of which has a distinct number of Li⁺ coordinating anions of 0, 1 and ≥ 2 in the primary solvation sheath, respectively. It is noteworthy that the classification of these Li⁺ solvates is slightly different from the conventional definition of solvent separated ion pair, contact ion pair or aggregate^{11,15,24,25}. The latter ones use the anion as the centre to count the coordinating Li⁺ number; instead, the SSL, LASP and LAC herein are proposed on the basis of Li⁺ solvation structures. In all electrolytes, LAC dominated the Li⁺ solvate species but the content of SSL and LASP (both classified as non-LAC) varied dramatically from one electrolyte to another, indicating substantial difference in ion dissociation degree. While almost no SSL and only a small proportion of LASP was observed in FDMB or F6DEE electrolytes, the non-LAC increased in the order of F5DEE (7.5% SSL + 11.9% LASP), F4DEE (9.5% SSL + 10.3% LASP), F3DEE (4.9% SSL + 31.4% LASP) and DEE (12.0% SSL + 37.6% LASP).

To explain structure–property correlations in depth, the following seven parameters/properties were leveraged to cross-validate the Li⁺–solvent interaction, solvation environments and properties measured in batteries (Fig. 3m): (1) Li⁺–solvent binding energies from DFT (Fig. 3a–f); (2) coordinating solvent numbers calculated from DOSY-NMR³² (Supplementary Table 2 and Supplementary Fig. 18); (3) non-LAC percentages from molecular dynamics

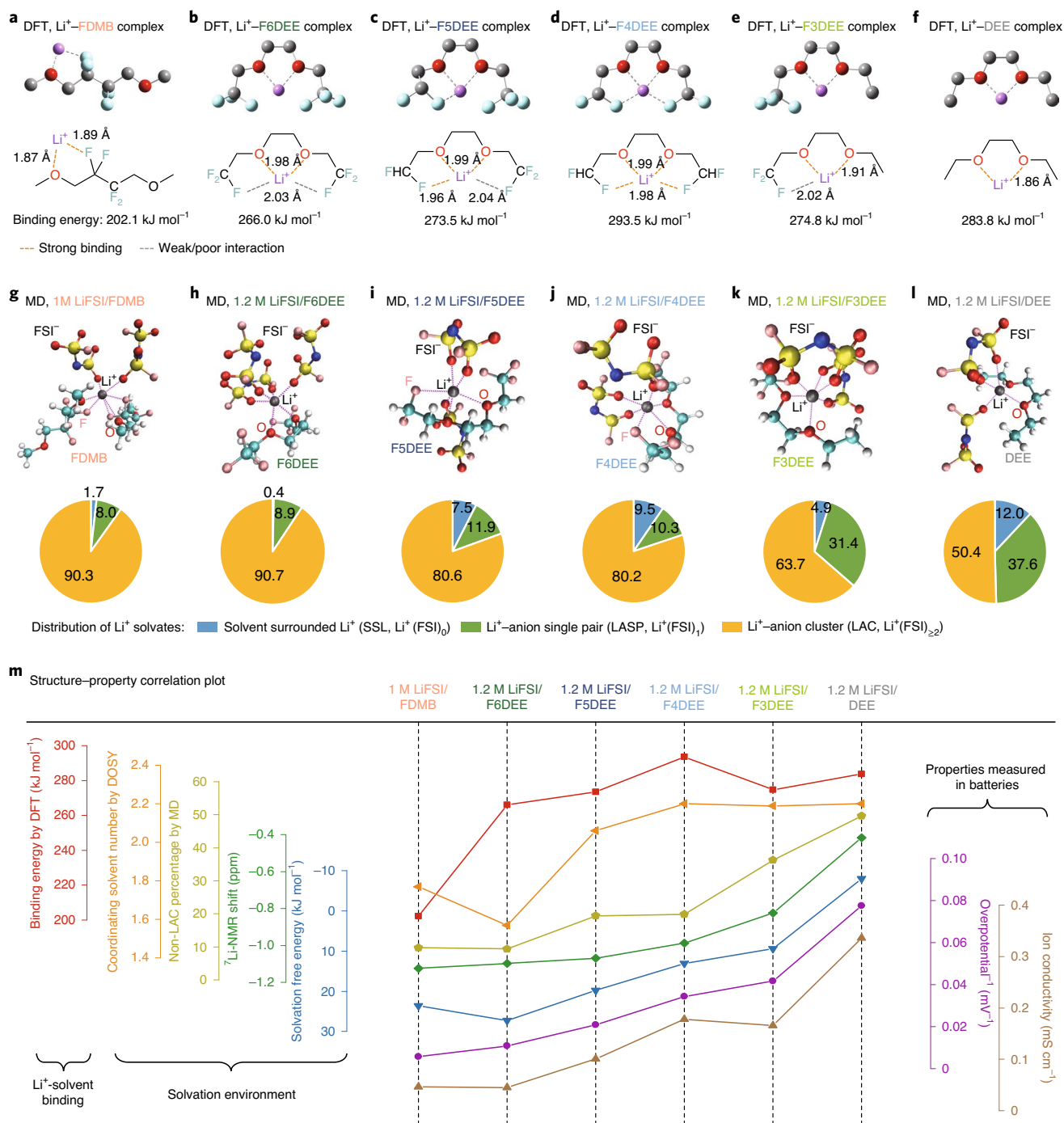


Fig. 3 | Theoretical and experimental study on the Li⁺ solvation structures and the structure-property correlations. **a-f**, Coordination structures and binding energies between one Li⁺ ion and one solvent molecule calculated using DFT. **a**, Li⁺-FDMB. **b**, Li⁺-F6DEE. **c**, Li⁺-F5DEE. **d**, Li⁺-F4DEE. **e**, Li⁺-F3DEE. **f**, Li⁺-DEE. **g-l**, Most probable solvation structures of the first Li⁺ solvation sheath from molecular dynamics (MD) simulations and the distribution of different Li⁺ solvates, that is, SSL, LASP and LAC. **g**, 1 M LiFSI/FDMB. **h**, 1.2 M LiFSI/F6DEE. **i**, 1.2 M LiFSI/F5DEE. **j**, 1.2 M LiFSI/F4DEE. **k**, 1.2 M LiFSI/F3DEE. **l**, 1.2 M LiFSI/DEE. The coordinating atoms on solvents (O and F) are labelled. Colour scheme of molecules: Li, dark grey; F, pink; O, red; C, light blue; N, navy; S, yellow; and H, white. **m**, Structure-property relationship plot of Li⁺-solvent binding, solvation environments and properties measured in batteries. The axes are shown in gradient height and each axis corresponds to the line chart with the same colour.

simulations (Fig. 3g-l and Supplementary Figs. 12-17); (4) chemical shifts of ⁷Li-NMR (Supplementary Fig. 19); (5) solvation free energies measured according to our recent work³¹ (Supplementary Fig. 20); (6) ionic conductivities shown in Fig. 2a and (7) overall cycling overpotentials of Li||Li cell extracted from Fig. 2c (converted to inversed overpotentials to better represent conduction property).

As plotted in Fig. 3m, these parameters follow similar trends against the choice of electrolytes. The main logic and rationales are as follows. First, more solvent molecules participating in the Li⁺ solvation sheath, that is, higher coordination numbers calculated by DOSY and more non-LAC solvates shown in molecular dynamics simulations, indicate greater binding ability and stronger

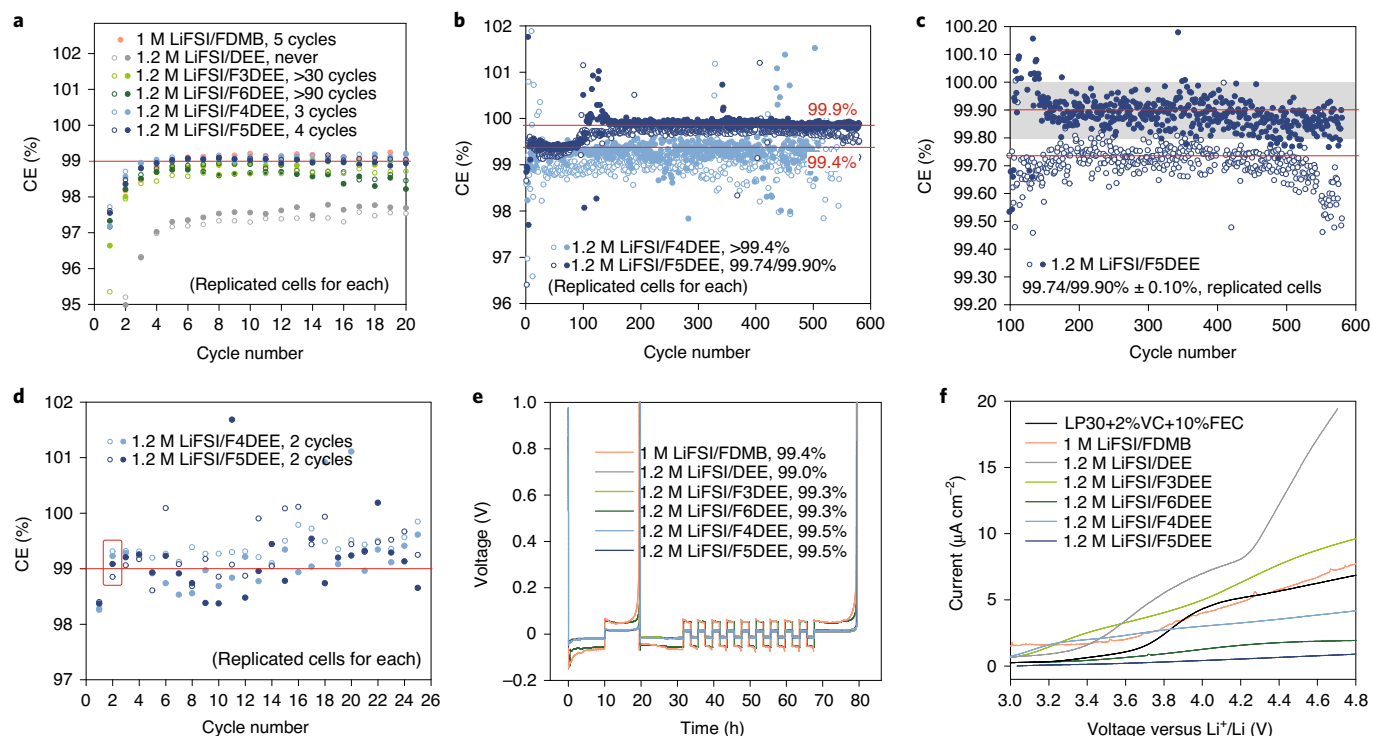


Fig. 4 | Li metal efficiency and high-voltage stability. **a–d**, Li||Cu half cells showing the Li metal initial activation at 0.5 mA cm^{-2} current density and 1 mAh cm^{-2} areal capacity (**a**), long cycling at 0.5 mA cm^{-2} and 1 mAh cm^{-2} (**b,c**), and initial activation at 0.5 mA cm^{-2} and 5 mAh cm^{-2} (**d**). Note: **c** is the zoomed-in plot of **b** from the 100th to the 600th cycles. **e**, Aurbach protocol^{43,44} in Li||Cu half cells to calculate the average Li metal CE (replicated results are shown in Supplementary Fig. 25). **f**, LSV of Li||Al half cells to show anodic stability and tolerance to Al corrosion. Note: replicated cell results are shown in **a–d**.

Li⁺–solvent interaction regardless of minor deviations in the trend^{24,42}; meanwhile, more coordinating solvents dispel electron-dense FSI[−] anions near Li⁺ and cause downfield (less negative) shift of ⁷Li-NMR peak. Second, solvation free energy is an overall estimation of the solvation environment³¹ (and the extent of Gibbs free energy decrease) between Li⁺ ions and surrounding species including both solvents and anions. Since the anion was fixed as FSI[−] in this work, stronger binding solvents will lead to more negative solvation energies. Third, at moderate concentrations where the vehicular mechanism dominates Li⁺ transport^{11,34}, strong binding solvents and good solvation reduce severe Li⁺–FSI[−] clustering (revealed by increasing non-LAC percentage and downfield ⁷Li shift), and result in separated mobile Li⁺ charge carriers^{11,24,25,36} that are responsible for the higher ionic conductivity and lower overall overpotential obtained in batteries. Last but not the least, it is worth noting that all the fluorinated-DEEs should still be classified as weakly solvating solvents; however, fine-tuning of fluorination enables sufficient solvation for fast transport while retaining electrode stabilities.

These arguments can be further cross-validated by attenuated total reflection–Fourier transform infrared spectroscopy (ATR–FTIR, Supplementary Fig. 21). All these factors and their correlations are consistent with each other and fill a broad range of scales ranging from molecular-level structure to mesoscopic Li⁺ solvation cluster statistics to bulk electrolyte properties, and finally to battery performance.

Enhanced Li metal and oxidative stability

Next, we investigated the electrolyte stability at Li metal anode and at high voltage separately. As shown in Fig. 4a, activation during initial cycles was tested using conventional Li||Cu half-cell setup at 0.5 mA cm^{-2} current density and 1 mAh cm^{-2} areal capacity.

The 1 M LiFSI/FDMB showed a five-cycle activation before ramping up to 99% CE²¹; while the DEE electrolyte never reached a CE of 99% (Supplementary Fig. 22). This confirms the argument above that DEE possesses fast ion conduction but sacrifices Li metal stability. In accord with our design, F3DEE and F6DEE solvents showed a substantial improvement over DEE, with activation periods measured to be around 30 and 90 cycles, respectively (Fig. 4a and Supplementary Fig. 22), confirming the benefit of fluorination. However, tens of activation cycles are still far from ideal case. The partially fluorinated electrolytes that contain $-\text{CHF}_2$ groups (Fig. 1a) performed much better, as the Li metal anode in F4DEE and F5DEE was activated within only three and four cycles, respectively. The CE of Li||Cu half cells using 1.2 M LiFSI/F5DEE was further boosted to roughly 99.9% when hard spring component (thus high pressure) was implemented in coin cells (Fig. 4b and Supplementary Fig. 23). Such a high average CE is reliable¹⁰ since the fluctuation range is as low as $\pm 0.1\%$ from the 100th to the 580th cycle even under ambient conditions (Fig. 4c and source data of Fig. 4). When the areal capacity was increased to 5 mAh cm^{-2} , the CE rapidly reached roughly 99.5% and the activation could even be completed by the second cycle (the second cycle CE > 99.3%), which is one of the fastest among the state-of-the-art electrolytes (Fig. 4d). At high current densities ($>4 \text{ mA cm}^{-2}$), the CE of Li||Cu cells showed a slight decrease and fluctuation (Supplementary Fig. 24). The benefit of fluorinated-DEE electrolytes was further validated by Aurbach CE measurements^{43,44}, in which F4DEE and F5DEE showed higher average CEs than other electrolytes (Fig. 4e and Supplementary Fig. 25).

The anodic stability was evaluated by linear sweep voltammetry (LSV) of Li||Al half cells, where the leakage current is a good metric to evaluate the corrosion of Al current collector^{7,23}. As shown in

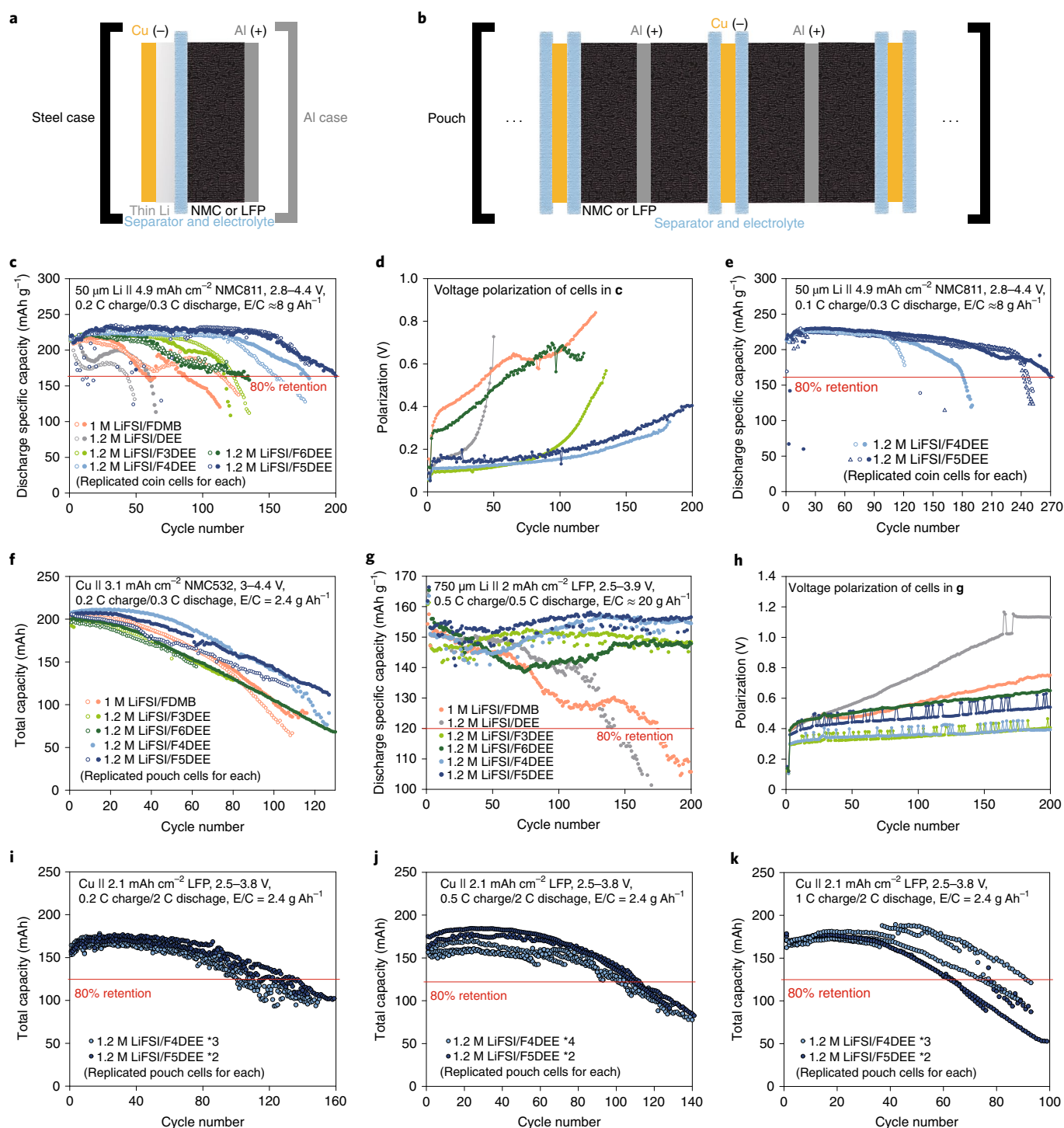


Fig. 5 | Full-cell performance of FDMB and fluorinated-DEE electrolytes. **a, b**, Cell structure of Li metal full battery (**a**) and anode-free pouch cell (**b**). **c, d**, Long-cycling performance (**c**) and voltage polarization (**d**) of thin Li||high-loading-NMC811 coin cells. Conditions: 50- μm thick Li, 4.9 mAh cm^{-2} NMC811, 2.8–4.4 V, 0.2 C charge 0.3 C discharge and electrolyte-to-cathode ratio (E/C) = 8 g Ah^{-1} . **e**, Long-cycling performance of thin Li||high-loading-NMC811 coin cells. Conditions: 50- μm thick Li, 4.9 mAh cm^{-2} NMC811, 2.8–4.4 V, 0.1 C charge 0.3 C discharge and $E/C = 8 \text{ g Ah}^{-1}$. **f**, Long-cycling performance of Cu||NMC532 industrial anode-free pouch cells. Conditions: 3.1 mAh cm^{-2} NMC532, 3–4.4 V, 0.2 C charge 0.3 C discharge and $E/C = 2.4 \text{ g Ah}^{-1}$. **g, h**, Long-cycling performance (**g**) and voltage polarization (**h**) of thick Li||microparticle-LFP coin cells. Conditions: 750- μm thick Li, 2 mAh cm^{-2} LFP, 2.5–3.9 V, 0.5 C charge, 0.5 C discharge with random 0.7 C discharge caused by instrument error and $E/C = 20 \text{ g Ah}^{-1}$. **i–k**, Long-cycling performance of Cu||microparticle-LFP anode-free pouch cells with different cycling rates. Conditions: 2.1 mAh cm^{-2} LFP, 2.5–3.8 V, $E/C = 2.4 \text{ g Ah}^{-1}$, slow charge fast discharge (**i**, 0.2 C charge 2 C discharge) and fast charge fast discharge (**j**, 0.5 C charge 2 C discharge, and **k**, 1 C charge 2 C discharge). Note: replicated cell results are shown in **c, e, f, i–k**. For NMC811, 1C = 200 mA g^{-1} ; for LFP, 1C = 155 mA g^{-1} .

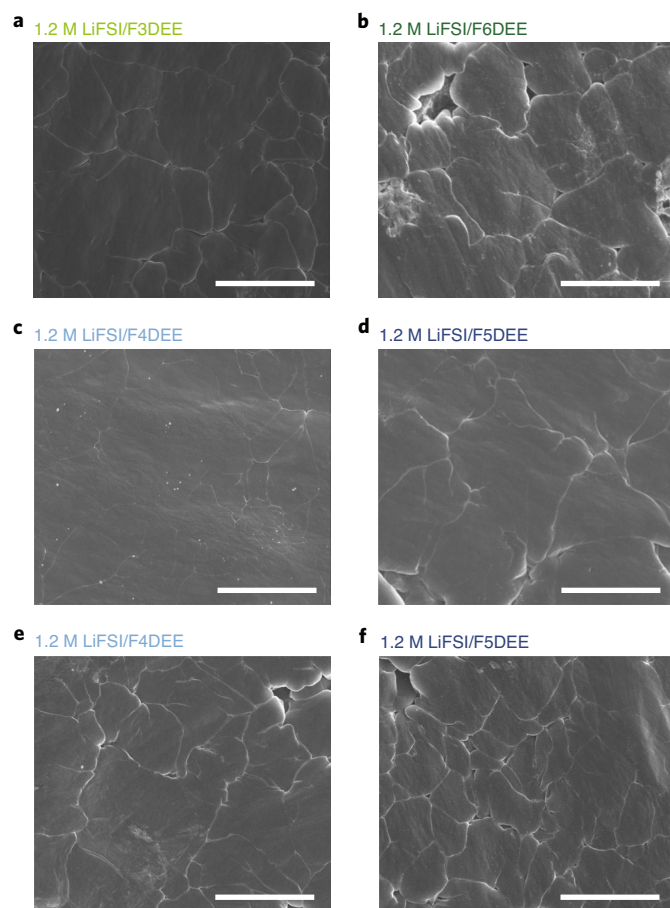


Fig. 6 | Li metal morphology in fluorinated-DEE electrolytes. **a–d**, Li metal morphology after 80 slow cycles (0.2 C slow charge, 0.3 C slow discharge) in Cu||microparticle-LFP anode-free pouch cells using 1.2 M LiFSI in F3DEE (**a**), F6DEE (**b**), F4DEE (**c**) and F5DEE (**d**), respectively. **e, f**, Li metal morphology after 90 fast cycles (1 C fast charge, 2 C fast discharge) in Cu||microparticle-LFP anode-free pouch cells using 1.2 M LiFSI in F4DEE (**e**) and F5DEE (**f**), respectively. Scale bars, 10 μm .

Fig. 4f, the DEE electrolyte was the most vulnerable at high voltage among these electrolytes; however, it was still far more stable against oxidation than DME (Supplementary Fig. 26). The leakage current evolution of FDMB²¹ under a high-voltage scan was similar to that of a conventional carbonate electrolyte (1 M LiPF₆ in ethylene carbonate/dimethyl carbonate (1/1) with 2% vinylene carbonate and 10% fluoroethylene carbonate, denoted as LP30 + 2%VC + 10%FEC), indicating reasonable high-voltage stability. As expected, the anodic stability of fluorinated-DEE electrolytes generally followed the trend of fluorination: F5DEE \cong F6DEE > F4DEE \gg F3DEE. Potentiostatic polarization tests at high voltage and molecular orbital energy level calculations provided similar trends (Supplementary Figs. 27 and 28).

Performance of Li metal and anode-free full cells

We proceeded to full cells to test the practicality of these developed electrolytes. Two types of Li metal battery are examined in this work: Li metal full cells using thin Li foil (Fig. 5a) and industrial anode-free jelly-roll pouch cells (Fig. 5b and Supplementary Table 3).

We first constructed Li metal full cells by pairing thin Li foil (50- μm thick, roughly 10 mAh cm⁻²) with an industrial high-loading NMC811 cathode (roughly 4.9 mAh cm⁻²). Using the

electrolyte-to-cathode ratio of around 8 gAh⁻¹, these coin cells were cycled at 0.2 C charge and 0.3 C discharge. These conditions are harsh among the state-of-the-art cells²⁶. The cycle life, which is defined as the cycle number before reaching 80% capacity retention, followed the trend of F5DEE > F4DEE \gg F6DEE \cong F3DEE > FDMB \gg DEE (Fig. 5c). All the cells showed high and stable full-cell CEs before failure (Supplementary Fig. 29a). The cycle life can be further correlated with voltage polarization⁴⁵, which is defined as the average voltage gap between charge and discharge. As shown in Fig. 5d and Supplementary Figs. 30 and 31, the poorly performing DEE showed drastic polarization increase with cycling; while the FDMB and F6DEE showed high yet slowly evolving overpotentials. The polarization of the F3DEE cell sharply increased at roughly 100 cycles, coinciding with when the cell suffered drastic capacity loss. Consistent with our expectation, the overpotentials of the long-cycling F4DEE and F5DEE full cells were low and stable throughout the whole cycle life. Using the best-performing electrolyte 1.2 M LiFSI/F5DEE, 50- μm thick Li||4.9 mAh cm⁻² NMC811 full cells maintained stable capacity for 270 cycles at a slow charging rate of 0.1 C, which are among the best high-loading Li metal full-cell performances^{12,13,26} (Fig. 5e and Supplementary Table 4). Similar to Li metal coin cells, the industrial anode-free pouch cells using single-crystal NMC532 showed the same trend of cycle life and impedance (Fig. 5f and Supplementary Fig. 32). Other types of cell or different cycling conditions also supported these conclusions (Supplementary Figs. 29 and 33–35).

To better evaluate the effect of fast ionic transport on full-cell performance, we further selected microparticle-LFP, a poorly conductive yet cost-effective cathode material^{46,47}. We started the investigation with thick Li||LFP half cells at a slightly higher cycling rate (0.5 C, 1 mA cm⁻²). As demonstrated in Fig. 5g, the highly conductive electrolytes, F3DEE, F4DEE and F5DEE, resulted in stable cycling with high capacities. The half cell using a less conductive yet Li-metal compatible F6DEE electrolyte delivered lower specific capacity. Although the capacity of both DEE and FDMB cells gradually diminished, we ascribed this to different mechanisms⁴⁵: for DEE, oxidation still happened at the charge voltage cut-off and the accumulation of side products increased the cell polarization (Fig. 5h and Supplementary Fig. 36), leading to capacity loss; for FDMB, its slow ionic conduction and continuously increasing overpotential due to residue SEI accumulation^{16,33} were responsible for its steady capacity decay, which was similar to the thin Li||NMC811 case (Fig. 5c,d and Supplementary Fig. 30). The benefit of stable and low overpotentials using F4DEE and F5DEE (Fig. 5h and Supplementary Fig. 36) was further verified by the rate capability tests of LFP half cells (Supplementary Fig. 37).

Industrial multilayer anode-free pouch cells using microparticle-LFP (with a practical loading of 2.1 mAh cm⁻²) were cycled at high rates to examine the limit of the developed electrolytes under stringent conditions. Compared to the lithium-nickel-manganese-cobalt-oxide (NMC) cathodes in anode-free cells, the LFP provides less Li excess inventory on the anode side during the first charging and consequently the cycle life will be shorter^{29,46,48–50}. Due to this material limitation, LFP-based anode-free batteries have seldom been studied in the community⁴⁶. As shown in Fig. 5i, at slow charge (0.2 C) and fast discharge (2 C) rate, the F4DEE and F5DEE electrolyte maintained roughly 110 and 140 cycles, respectively, before reaching 80% capacity. Faster charging rates were further applied. At a 0.5 C charge and 2 C discharge rate, roughly 110 cycles were achieved for both F4DEE and F5DEE (Fig. 5j). When the charging rate was boosted to 1 C, the faster conducting F4DEE electrolyte outperformed F5DEE, enabling 80–90 cycles before fading (Fig. 5k). These fast-cycling conditions are harsh for low-cost microparticle-LFP-based anode-free pouch cells, and the cycle lives are among the state-of-the-art (Supplementary Table 5). Performance of anode-free LFP pouch cells under other

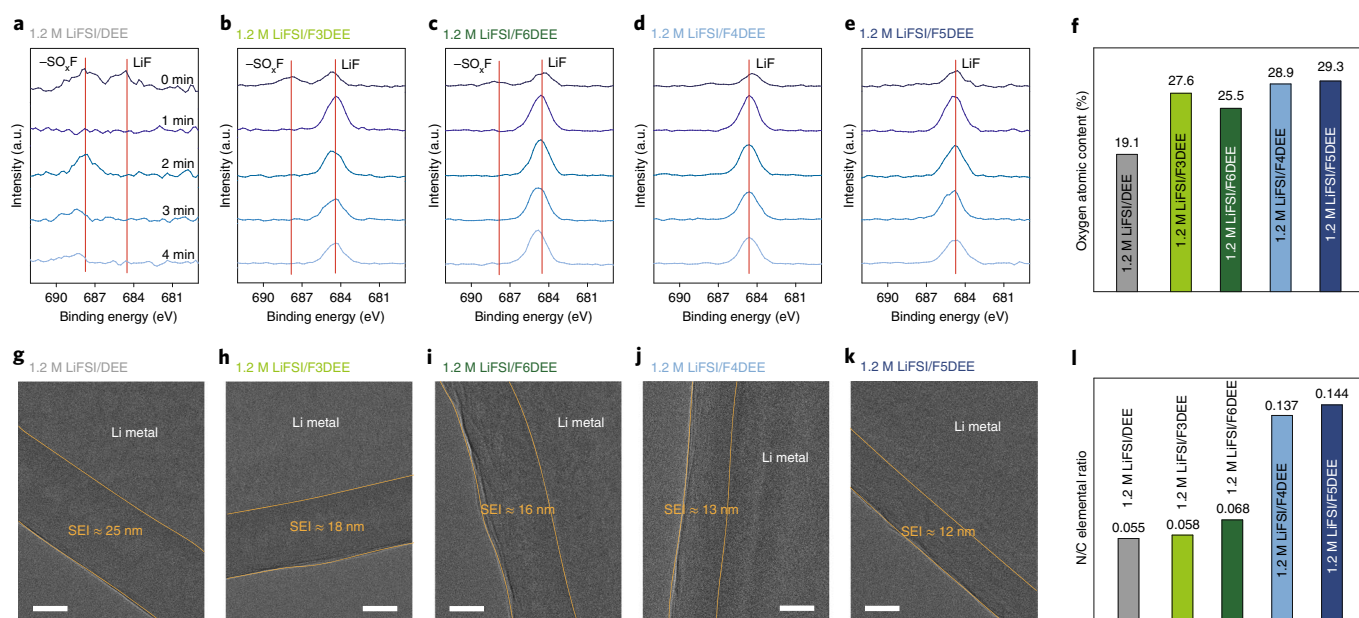


Fig. 7 | SEI examination in fluorinated-DEE electrolytes. a–e, XPS F1s depth profiles (by sputtering for different lengths of time) of cycled Li metal electrodes using 1.2 M LiFSI in DEE (**a**), F3DEE (**b**), F6DEE (**c**), F4DEE (**d**) and F5DEE (**e**), respectively. a.u., arbitrary units. **f**, Oxygen atomic contents by XPS of cycled Li metal electrodes in fluorinated-DEE electrolytes. **g–k**, Cryo-TEM images of 0.1 mAh cm⁻² deposited Li metal using 1.2 M LiFSI in DEE (**g**), F3DEE (**h**), F6DEE (**i**), F4DEE (**j**) and F5DEE (**k**), respectively. Scale bars, 10 nm. **l**, N/C elemental ratios by cryo-EDS of Li metal deposits in fluorinated-DEE electrolytes.

cycling conditions also supported our arguments (Supplementary Fig. 38). Moreover, no gassing issue was observed for these pouch cells after fast cycling even though no degassing procedure was implemented, indicating high safety and ease of manufacturing (Supplementary Fig. 39).

Li morphology, SEI structure and cathode characterization

Li metal morphology and SEI properties are crucial for Li metal battery performance. Anode-free pouch cells after cycling were chosen here for scanning electron microscope (SEM) examination since they generated the Li deposits under realistic full-cell conditions. After 80 cycles at 0.2 C charge and 0.3 C discharge, the Cu||LFP pouch cells were charged to the upper cut-off voltage, that is, Li⁺ ions in LFP cathode were fully deposited as metallic Li on the anode. As shown in Fig. 6a–d and Supplementary Figs. 40 and 41, chunky and desired Li deposits were observed in all fluorinated-DEE electrolytes. However, careful examination revealed more favourable Li deposition in F4DEE and F5DEE electrolytes where the Li deposits had characteristic length scales much larger than 10 μm (Fig. 6c,d). In particular, the Li deposits in the F4DEE electrolyte were almost flat with few grain boundaries, and such morphology was consistent with its long cycle life in anode-free cells. The diameters of Li deposits in F3DEE and F6DEE, in contrast, were slightly lower than 10 μm (Fig. 6a,b). Under fast-cycling condition (1 C charge 2 C discharge), F4DEE and F5DEE maintained chunky Li morphology, which matched well with their outstanding cycle life at a high rate (Fig. 6e,f and Supplementary Fig. 41). The SEM images taken under other cycling conditions (Supplementary Fig. 41) or with Cu||NMC532 pouch cells (Supplementary Fig. 42) exhibited similar features.

Next, X-ray photoelectron spectroscopy (XPS) was used to examine the SEI compositions. The XPS F1s spectra with sputtering showed a distinct difference between DEE and fluorinated-DEEs, in which the latter contained clear LiF signal while the former only showed trivial signal for this species (Fig. 7a–e). Although uniformly distributed LiF throughout depth profiling dominated the surface fluorine species in all fluorinated-DEEs, the anion

species –SO_xF remained on the top surface of Li metal in F3DEE and F6DEE electrolytes, indicating incomplete anion decomposition or passivation. The LiF-rich, vertically homogeneous SEI in F4DEE and F5DEE corroborates with their outstanding Li metal efficiency (Fig. 4a–e). Depth profiles of other representative elements demonstrated similar observations (Supplementary Figs. 43–45). Such a fine difference agreed well with our careful design rationales evolving from F3DEE/F6DEE to F4DEE/F5DEE. Furthermore, the O1s spectra showed that Li₂O was present (Supplementary Fig. 43) and the oxygen content was higher in the fluorinated-DEE electrolytes especially in the best-performing F4DEE and F5DEE, indicating an oxygen-rich SEI (Fig. 7f). Such a robust SEI was reported to be beneficial to Li metal efficiency as well as interfacial Li⁺ ion transport^{51,52}.

We further performed cryogenic transmission electron microscopy (cryo-TEM) and corresponding energy-dispersive X-ray spectroscopy (cryo-TEM EDS or cryo-EDS) to unveil the fine structural and local chemical information of compact direct SEIs^{33,53} on Li metal surface. All compact SEIs in these electrolytes exhibited thin, uniform and amorphous nanostructure under cryo-TEM (Fig. 7g–k and Supplementary Fig. 46); however, the SEIs in F4DEE and F5DEE were the thinnest, corroborating with their high CE and fast activation. The nitrogen-to-carbon (N/C) ratio by cryo-EDS served as an indicator of anion-derived favourable SEIs since FSI⁻ is solely the source of N element in these electrolytes. Much higher N/C ratios were observed in F4DEE and F5DEE (Fig. 7l), corresponding to more anion-derived SEIs. These facts were cross-validated by other elemental ratios, especially the sulfur-to-carbon (S/C) and fluorine-to-carbon (F/C) (Supplementary Figs. 47 and 48), again indicating anion-derived inorganic-rich SEIs^{16,21,33}.

Robust cathode–electrolyte interphase and suppression of cathode cracking are also critical for stable full-cell operation²³. We analysed the elemental composition of cathode–electrolyte interphase by XPS and found that high C and F content yet negligible Ni species were observed on the cathode surface when using FDMB and fluorinated-DEE electrolytes, confirming their cathode protection

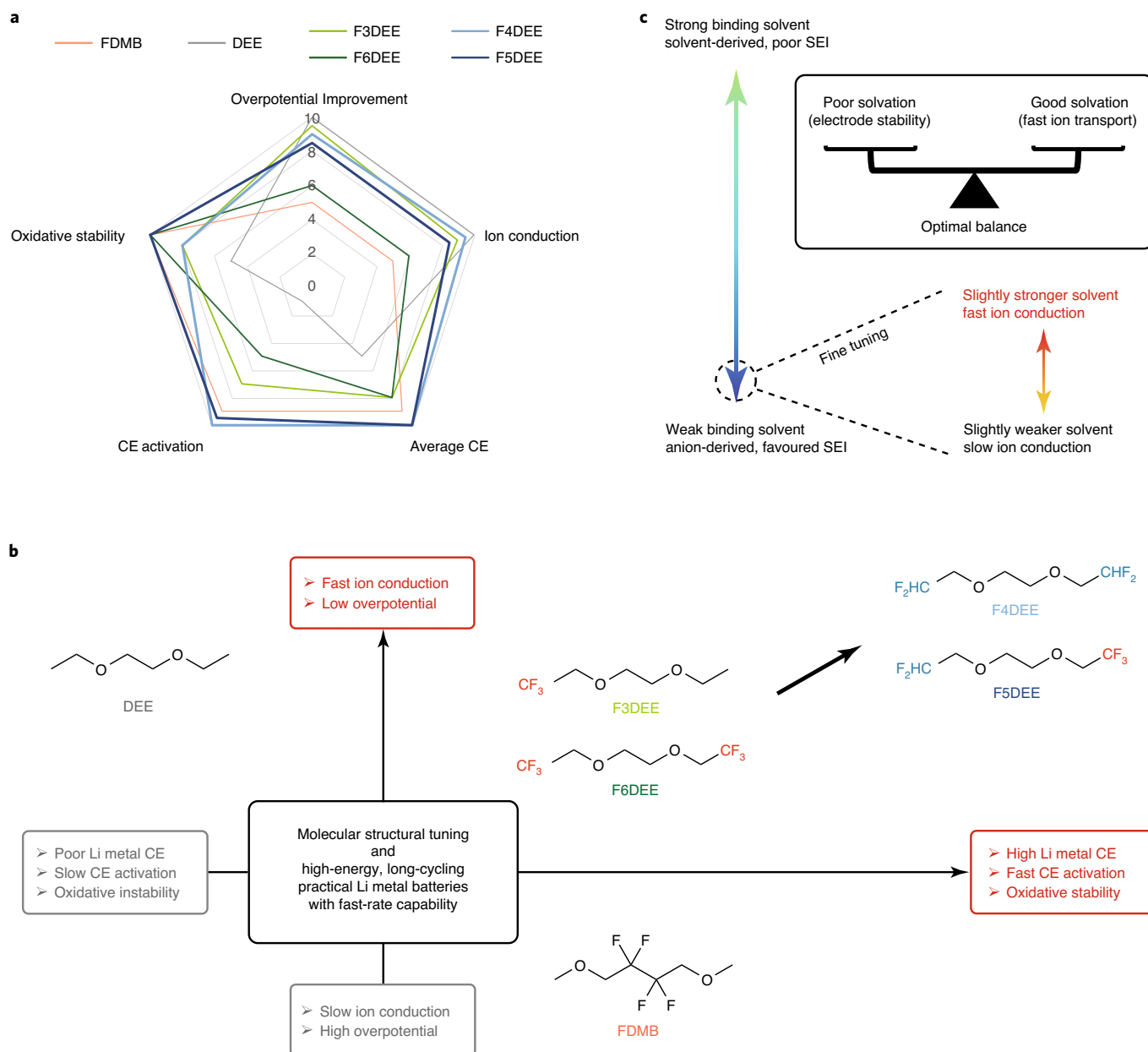


Fig. 8 | Summary and overall evaluation of fluorinated-DEE electrolytes. **a**, Radar plot evaluating the developed electrolytes. The ratings between 1 and 10 are given according to the measured performance of each electrolyte. The rating of 1 represents extremely slow ionic conduction, large/unstable overpotential, poor Li metal CE, slow CE activation or oxidative instability; while 10 stands for the opposite, ideal properties. The rating values are provided in the source data. **b**, Development directions for good electrolytes: fast ion conduction, low overpotential, high Li metal efficiency, fast CE activation and high oxidative stability. **c**, A scheme showing the principles in this work: finding an optimal balance between good and poor solvation, that is, searching relatively strong solvents among weakly binding ones.

effect^{13,23} (Supplementary Fig. 49). Furthermore, NMC811 particles showed limited intergranular cracking after cycling, again indicating the stability of cathode towards these developed electrolytes (Supplementary Fig. 50).

Overall evaluation of fluorinated-DEE electrolytes

We evaluated the electrolytes studied in this work from five angles: bulk ionic conduction, overpotential/polarization improvement, Li metal CE, activation speed and oxidative stability (Fig. 8a). The DEE electrolyte exhibits advantageous ionic conduction but poor Li metal CE, slow activation and oxidative instability; conversely, FDMB shows improvement over all the above aspects except for worse ionic

conduction and poor interfacial transport. The fluorinated-DEEs all show more balanced behaviour; however, F4DEE and F5DEE outperform F3DEE and F6DEE, which confirms our design logic (Fig. 8b). Our study suggests that the strongest binding solvents (such as DEE) are not necessarily desirable; instead, a balance needs to be achieved by finely modulating the molecular structure of weakly binding solvents, which ensures both electrode stability and sufficient solvation for fast transport (Fig. 8c).

Conclusions

In summary, we investigated a family of fluorinated-DEE based electrolytes for Li metal batteries, in which the partially

fluorinated $-\text{CHF}_2$ group was identified and rationalized as the designer choice. The developed electrolytes, especially F4DEE and F5DEE, simultaneously possess high ionic conductivity, low and stable interfacial transport, reproducibly high Li metal efficiency (up to 99.9% with only $\pm 0.1\%$ fluctuation for 1.2 M LiFSI/F5DEE in Li||Cu half cells), record-fast activation ($\text{CE} > 99.3\%$ within from the second cycle in Li||Cu half cells) and high-voltage stability. These features enable long cycle life of Li metal batteries and anode-free pouch cells under lean electrolyte and realistic testing conditions. Thorough morphological characterization and SEI examination revealed flat Li deposition as well as an ideal anion-derived SEI. We also conducted a systematic study on the structure–performance relationships in these electrolytes via multiple theoretical and experimental tools, in which crucial properties including Li^+ –solvent coordination, solvation structure and battery performance were cross-validated and their correlations were thoroughly explained. Our work emphasizes the critical yet less-studied direction, fast ion conduction, in the Li metal battery electrolyte research. It is critical to achieve a balance between fast ion conduction and electrode stability through fine-tuning the solvation ability of the solvent, and molecular design and synthetic tools play important roles here. We believe that rational molecular-level design and chemical synthesis can endow the electrolyte field with more opportunities in the future.

Methods

General materials. 2,2,3,3-Tetrafluoro-1,4-butanediol, 2-(2,2,2-trifluoroethoxy) ethanol, 2,2-difluoroethanol, ethyl p-toluenesulfonate, 2,2,2-trifluoroethyl p-toluenesulfonate and 2,2-difluoroethyl p-toluenesulfonate were purchased from SynQuest. Ethylene carbonate (98%), sodium hydride (60% in mineral oil), methyl iodide, tetraglyme and other general reagents were purchased from Sigma-Aldrich, Fisher Scientific or TCI. All chemicals for reactions were used without further purification. LiFSI was obtained from Guangdong Canrd New Energy Technology and Arkema. DME (99.5% over molecular sieves) and DEE (also denoted as ethylene glycol diethyl ether, 99%) were purchased from Acros. Anhydrous vinylene carbonate and fluoroethylene carbonate were purchased from Sigma-Aldrich. The commercial carbonate electrolytes LP30 and LP40 were purchased from Gotion. The commercial Li battery separator Celgard 2325 (25- μm thick, polypropylene/polyethylene/polypropylene) was purchased from Celgard and used in all coin cells. Thick Li foil (roughly 750- μm thick) and Cu current collector (25- μm thick) were purchased from Alfa Aesar. Thin Li foils (roughly 50- and 20- μm thick, supported on Cu substrate) were purchased from China Energy Lithium. Commercial LFP and NMC532 cathode sheets were purchased from MTI, and NMC811 cathode sheets were purchased from Targray (roughly 2.2 and 4.9 mAh cm^{-2} areal capacity). Industrial dry Cu||NMC532 and Cu||LFP pouch cells were purchased from Li-Fun Technology. Other battery materials, such as 2032-type coin-cell cases, springs and spacers, were all purchased from MTI.

Syntheses. FDMB was synthesized using the same protocol as our previous report²¹. To a 1,000-ml round-bottom flask, 64 g of 2,2,3,3-tetrafluoro-1,4-butanediol and 400 ml of anhydrous tetrahydrofuran were added, and the solution was cooled to 0 °C by ice bath to stir for 10 min. Then 40 g of NaH (60% in mineral oil) was added in batches and the suspension was stirred at 0 °C for 30 min. Next, 140 g of methyl iodide was added slowly into the stirring suspension and then the ice bath was removed to allow the suspension to warm up to room temperature. After stirring at room temperature for 2 h, the flask was slowly heated up to 60 °C to reflux overnight. After the completion of reaction, the flask was allowed to cool down to room temperature, the mixture was filtered off and the solvents were removed under vacuum. The crude product underwent vacuum distillation (roughly 45 °C under 1 kPa) three times to yield the final product as a colourless liquid.

For 2-(2,2-Difluoroethoxy)ethanol (Supplementary Figs. 51–54), in a 1,000-ml round-bottom flask were added 150 g of 2,2-difluoroethanol, 140 g of ethylene carbonate, 8 g of NaOH and 200 ml of tetraglyme. Under nitrogen atmosphere, the suspension was heated to 140 °C to stir for 48 h. The suspension was then distilled under vacuum (roughly 65 °C under 1 kPa) three times to yield roughly 100 g of colourless liquid as the product. Yield: roughly 43%. ¹H-NMR (400 MHz, CDCl_3 , δ/ppm): 6.00–5.70 (tt, 2H), 3.71–3.60 (m, 6H), 3.05 (s, 1H). ¹³C-NMR (100 MHz, CDCl_3 , δ/ppm): 116.96–112.17, 73.63, 70.74–70.20, 61.67. ¹⁹F-NMR (376 MHz, CDCl_3 , δ/ppm): –125.74––125.96 (dt, 4F).

For F3DEE (Supplementary Figs. 51 and 55–57), to a 1,000-ml round-bottom flask 22 g of NaH (60% in mineral oil) and 400 ml of anhydrous tetrahydrofuran were added, and the suspension was cooled to 0 °C by ice bath to stir for 10 min. Then 56 g of 2-(2,2,2-trifluoroethoxy)ethanol was added dropwise

and the suspension was further stirred at 0 °C for 30 min. Next, 93 g of ethyl p-toluenesulfonate was added in batches and the ice bath was removed to allow the suspension to warm up to room temperature. After stirring at room temperature for 2 h, the flask was slowly heated up to 60 °C to reflux overnight. After the completion of reaction, the flask was allowed to cool down to room temperature and 200 ml of deionized water was slowly added into the suspension to dissolve all solids. The remaining tetrahydrofuran in the resulting solution was removed under vacuum, and then the solution was extracted with 500 ml of dichloromethane three times. The dichloromethane layer was washed with brine, dried by anhydrous MgSO_4 and the solvents were removed under vacuum. The crude product underwent vacuum distillation (roughly 40 °C under 1 kPa) three times to yield roughly 43 g of colourless liquid as the product. Yield: roughly 64%. ¹H-NMR (400 MHz, CDCl_3 , δ/ppm): 3.94–3.87 (q, 2H), 3.77–3.59 (m, 4H), 3.55–3.50 (q, 2H), 1.23–1.19 (3H). ¹³C-NMR (100 MHz, CDCl_3 , δ/ppm): 128.44–120.10, 72.25, 70.06, 69.48–68.47, 67.00, 15.34. ¹⁹F-NMR (376 MHz, CDCl_3 , δ/ppm): –74.66––74.71 (t, 3F). Electrospray ionization–mass spectrometry (ESI–MS) calculated $[\text{M} + \text{H}^+]$: 173.16; found: 173.32.

For F6DEE (Supplementary Figs. 51 and 58–60), the same procedure as for F3DEE synthesis was adopted, except that 93 g of ethyl p-toluenesulfonate was replaced by 120 g of 2,2,2-trifluoroethyl p-toluenesulfonate. The crude product underwent vacuum distillation (roughly 40 °C under 1 kPa) three times to yield roughly 50 g of colourless liquid as the product. Yield: roughly 57%. ¹H-NMR (400 MHz, CDCl_3 , δ/ppm): 3.92–3.86 (q, 4H), 3.80 (s, 4H). ¹³C-NMR (100 MHz, CDCl_3 , δ/ppm): 128.28–119.95, 72.14, 69.53–68.52. ¹⁹F-NMR (376 MHz, CDCl_3 , δ/ppm): –74.97––75.01 (t, 6F). ESI–MS calculated $[\text{M} + \text{H}^+]$: 227.13; found: 227.20.

For F4DEE (Supplementary Figs. 51 and 61–63), the same procedure as for F3DEE synthesis was adopted, except that 56 g of 2-(2,2,2-trifluoroethoxy) ethanol was replaced by 50 g of 2-(2,2-difluoroethoxy)ethanol and 93 g ethyl p-toluenesulfonate was replaced by 110 g of 2,2-difluoroethyl p-toluenesulfonate. The crude product underwent vacuum distillation (roughly 60 °C under 1 kPa) three times to yield roughly 45 g of colourless liquid as the product. Yield: roughly 60%. ¹H-NMR (400 MHz, CDCl_3 , δ/ppm): 6.00–5.70 (tt, 2H), 3.73–3.68 (td, 4H), 3.69 (s, 4H). ¹³C-NMR (100 MHz, CDCl_3 , δ/ppm): 116.80–112.01, 71.35, 70.74–70.20. ¹⁹F-NMR (376 MHz, CDCl_3 , δ/ppm): –125.35––125.57 (dt, 4F). ESI–MS calculated $[\text{M} + \text{H}^+]$: 191.15; found: 191.22.

For F5DEE (Supplementary Figs. 51 and 64–66), the same procedure as for F3DEE synthesis was adopted, except that 56 g of 2-(2,2,2-trifluoroethoxy) ethanol was replaced by 50 g of 2-(2,2-difluoroethoxy)ethanol and 93 g of ethyl p-toluenesulfonate was replaced by 120 g of 2,2-difluoroethyl p-toluenesulfonate. The crude product underwent vacuum distillation (roughly 60 °C under 1 kPa) three times to yield roughly 62 g of colourless liquid as the product. Yield: roughly 75%. ¹H-NMR (400 MHz, CDCl_3 , δ/ppm): 6.01–5.71 (tt, 1H), 3.92–3.85 (td, 2H), 3.79–3.67 (m, 6H). ¹³C-NMR (100 MHz, CDCl_3 , δ/ppm): 128.09–119.74, 116.74–111.94, 71.83, 71.41, 70.82–70.28, 69.21–68.19. ¹⁹F-NMR (376 MHz, CDCl_3 , δ/ppm): –74.53––74.58 (t, 3F), –125.37––125.59 (dt, 2F). ESI–MS calculated $[\text{M} + \text{H}^+]$: 209.14; found: 209.31.

Electrolyte preparation. LiFSI (2,244 mg) was dissolved in 10 ml of DEE or fluorinated-DEEs to obtain the respective 1.2 M LiFSI electrolyte. LiFSI (1,122 mg) was dissolved in 6 ml of DME or FDMB to obtain 1 M LiFSI/DME and 1 M LiFSI/FDME, respectively. All the electrolytes were prepared and stored in an argon-filled glovebox (Vigor, oxygen <0.5 ppm, water <0.1 ppm) at room temperature.

Theoretical calculations. The molecular geometries for the ground states were optimized by DFT at the B3LYP/6–311G+ (*d, p*) level, and then the energy, orbital levels and electrostatic potential surfaces of molecules were evaluated at the B3LYP/6–311G+ (*d, p*) level as well. All DFT calculations were carried out with Gaussian16 on Sherlock server at Stanford University.

Molecular dynamics simulations were carried out using Gromacs 2018 program⁵⁴, with electrolyte molar ratios taken from experimental results. Molecular forces were calculated using the Optimized Potentials for Liquid Simulations all atom force field⁵⁵. Topology files and bonded and Lennard–Jones parameters were generated using the LigParGen server⁵⁶. Atomic partial charges were calculated by fitting the molecular electrostatic potential at atomic centres in Gaussian16 using the Møller–Plesset second-order perturbation method with a cc-pVTZ basis set⁵⁷. Due to the use of a non-polarizable force field, partial charges for charged ions were scaled by 0.8 to account for electronic screening, which has been shown to improve predictions of interionic interactions⁵⁸. The simulation procedure consisted of an energy minimization using the steepest descent method followed by an 8-ns equilibration step using a Berendsen barostat and a 40-ns production run using a Parrinello–Rahman barostat, both at a reference pressure of 1 bar with timesteps of 2 fs. A Nose–Hoover thermostat was used throughout with a reference temperature of 300 K. The particle mesh Ewald method was used to calculate electrostatic interactions, with a real space cut-off of 1.2 nm and a Fourier spacing of 0.12 nm. The Verlet cut-off scheme was used to generate pairlists. A cut-off of 1.2 nm was used for non-bonded Lennard–Jones interactions. Periodic boundary conditions were applied in all directions. Bonds with hydrogen atoms were constrained. Convergence of the system energy, temperature and box size were checked to verify equilibration. The final 30 ns of the production run were

used for the analysis. Density profiles and RDFs were generated using Gromacs, while visualizations were generated with VMD³⁹. Solvation shell statistics were calculated using the MDAnalysis Python package⁴⁰ by histogramming the observed first solvation shells for Li⁺ ions during the production simulation, using a method similar to our previous work²¹. The cut-off distance for each species in the first solvation shell was calculated from the first minimum occurring in the RDF (referenced to Li⁺ ions) after the initial peak. The SSL, LASP and LAC each has a distinct number of Li⁺ coordinating anions of 0, 1 and ≥ 2 (2–5 in this work), respectively (Supplementary Figs. 12–17), in the first solvation sheath, and the percentage of each was counted based on this criterion.

General material characterizations. ¹H-, ¹³C- and ¹⁹F-NMR spectra were recorded on a Varian Mercury 400 MHz NMR spectrometer and ⁷Li-NMR spectra were recorded on a UI 500 MHz NMR spectrometer at room temperature. Solvation free energies were measured according to our recent work²¹. ATR-FTIR spectra were measured using a Nicolet iS50 with a diamond attenuated total reflectance attachment. FEI Magellan 400 XHR and Thermo Fisher Scientific Apreo S LoVac were used for taking SEM images. Ion milling was done by Fischione Model 1061 Ion Mill. For XPS measurements, each Li foil (after ten Li||Li cell cycles) or NMC811 cathode (after 30 Li||NMC811 cell cycles) was washed with DME for 30 s to remove the remaining electrolytes. The samples were transferred and sealed into the XPS holder in the argon-filled glovebox. The XPS profiles were collected with a PHI VersaProbe 1 scanning XPS microprobe. Viscosity measurements were carried out using an Ares G2 rheometer (TA Instruments) with an advanced Peltier system at 25.0 °C.

Cryo-TEM and cryo-TEM EDS. A Thermo Fisher Titan 80-300 environmental transmission electron microscope at an accelerating voltage of 300 kV and a Gatan 626 side-entry holder were used for cryo-TEM and cryo-TEM EDS experiments. Cryo-TEM sample preparations prevent air and moisture exposure and reduce electron beam damage, as described previously⁴³. The TEM is equipped with an aberration corrector in the image-forming lens, which was tuned before imaging. Cryo-TEM images were acquired by a Gatan K3 IS direct-detection camera in the electron-counting mode. Cryo-TEM images were taken with an electron dose rate of around 100 e⁻ Å⁻² s⁻¹, and a total of five frames were taken with 0.1 s per frame for each image.

DOSY-NMR. For sample preparation, benzene-d₆ was placed in an external coaxial insert and the ¹H chemical shifts were referenced to it at 7.16 ppm. In an argon glovebox, 20 μl of anhydrous toluene was mixed into 300 μl of sample solution and then added into the NMR tube. The cap of NMR tube was sealed by parafilm to avoid moisture penetration during the DOSY-NMR experiment.

The measurement methods and parameters were as follows: all DOSY-NMR experiments were carried out using a 500 MHz Bruker Avance I spectrometer equipped with a z axis gradient amplifier and a 5-mm BBO probe with a z axis gradient coil that is capable of a maximum gradient strength at 0.535 T m⁻¹. The spectrometer frequencies for ¹H- and ⁷Li- experiments were 500.23 and 194.41 MHz, respectively. ¹H- and ⁷Li-pulsed field gradient (PFG) measurements were performed to determine the diffusion coefficients for the solvents and electrolytes in this work. Both ¹H- and ⁷Li-PFG measurements were performed at 298 K using the standard dstebpgp3s Bruker pulse program, using a double stimulated echo sequence, bipolar gradient pulses for diffusion and three spoil gradients. Apparent diffusion coefficients were calculated by fitting peak integrals to the Stejskal–Tanner equation modified for the dstebpgp3s pulse sequence⁶¹, and the signal attenuation due to diffusion as a function of gradient strength was in good agreement with the numerical fits for all data sets (Supplementary Table 2 and Supplementary Fig. 18). The sample temperature was calibrated to 298 K using the ¹H chemical shifts of the ethylene glycol sample⁶². Similarly, the performance for the PFGs was calibrated at 298 K using dstebpgp3s sequence and the ethylene glycol sample⁶³. The PFG experiments were conducted using the following set of parameters. ¹H-PFG of solvents: diffusion delay (Δ , d20) = 40 ms, gradient pulse duration (δ , 2 × p30) = 2 ms, gradient recovery delay (d16) = 200 μs, array of gradient strength (gpz6) = 5% to 80% with 12 linear increments, recycling delay (d1) = 2 s and high power 90° pulse (p1) = 9 μs. ¹H-PFG of electrolytes: diffusion delay (Δ , d20) = 150 ms, gradient pulse duration (δ , 2 × p30) = 2 ms, gradient recovery delay (d16) = 200 μs, array of gradient strength (gpz6) = 5 to 80% with linear 12 increments, recycling delay (d1) = 2 s and high power 90° pulse (p1) = 9 μs. ⁷Li-PFG of electrolytes: diffusion delay (Δ , d20) = 500 ms, gradient pulse duration (δ , 2 × p30) = 4 ms, gradient recovery delay (d16) = 200 μs, array of gradient strength (gpz6) = 5% to 80% with linear 12 increments, recycling delay (d1) = 2 s and high power 90° pulse (p1) = 13 μs.

Electrochemical measurements. All battery components used in this work were commercially available and all electrochemical tests were carried out in a Swagelok-cell, 2032-type coin-cell or pouch-cell configuration. All coin cells were fabricated in an argon-filled glovebox, and one layer of Celgard 2325 was used as a separator. The EIS, Li⁺ transference number, LSV and pouch-cell cycling were carried out on a Biologic VMP3 system. The cycling tests for coin cells and some pouch cells were carried out on an Arbin instrument. The EIS measurements

were taken over a frequency range of 1 MHz to 100 mHz. For the Li⁺ transference number measurements, 10 mV constant voltage bias was applied to Li||Li cells. The cathodic cyclic voltammetry tests were carried out over a voltage range of –0.1 to 2 V for one cycle in Li||Cu cells, while the anodic LSV tests were over a voltage range of 2.5 to 6.5 V in Li||Al cells. For Li||Li symmetric-cell cycling, 1 mA cm⁻² current density and 1 mAh cm⁻² areal capacity were applied. For Li||Cu half-cell CE tests, ten precycles between 0 and 1 V were initialized to clean the Cu electrode surface, and then cycling was done by depositing 1 (or 5) mAh cm⁻² of Li onto the Cu electrode followed by stripping to 1 V. The CE is calculated by dividing the total stripping capacity by the total deposition capacity after the formation cycles. For the Aurbach CE test^{43,44}, a standard protocol was followed: (1) perform one initial formation cycle with Li deposition of 5 mAh cm⁻² on Cu under 0.5 mA cm⁻² current density and stripping to 1 V; (2) deposit 5 mAh cm⁻² Li on Cu under 0.5 mA cm⁻² as a Li reservoir; (3) repeatedly strip/deposit Li of 1 mAh cm⁻² under 0.5 mA cm⁻² for ten cycles; (4) strip all Li to 1 V. The Li||NMC and Cu||NMC full cells were cycled with the following method (unless specially listed): after the first two activation cycles at 0.1 C charge/discharge (or 0.1 C charge 0.3 C discharge for anode-free pouch cells), the cells were cycled at different rates. Then a constant-current-constant-voltage protocol was used for cycling: cells were charged to top voltage and then held at that voltage until the current dropped below 0.1 C. The NMC811 coin cells were cycled between 2.8 and 4.4 V and the single-crystal NMC532 pouch cells were cycled between 3.0 and 4.4 V. The Li||LFP and Cu||LFP full cells were cycled with the following method (unless specially listed): after the first two activation cycles at 0.1 C charge/discharge (or 0.1 C charge 2 C discharge for anode-free pouch cells), the cells were cycled at different rates. The LFP coin cells were cycled between 2.5 and 3.9 V and the LFP pouch cells were cycled between 2.5 and 3.8 V, or between 2.5 and 3.7 V. All pouch cells were clamped in woodworking vises to a rough pressure of 1,000 kPa and cycled under ambient conditions without temperature control.

Data availability

All relevant data are included in the paper and its Supplementary Information. Source data are provided with this paper.

Code availability

The Python script and rationale for analysing the Li⁺ solvation structures are available at <https://github.com/xianshine/LiSolvationStructure>.

Received: 19 August 2021; Accepted: 24 November 2021;

Published online: 13 January 2022

References

- Liu, J. et al. Pathways for practical high-energy long-cycling lithium metal batteries. *Nat. Energy* **4**, 180–186 (2019).
- Cao, Y., Li, M., Lu, J., Liu, J. & Amine, K. Bridging the academic and industrial metrics for next-generation practical batteries. *Nat. Nanotechnol.* **14**, 200–207 (2019).
- Tikekar, M. D., Choudhury, S., Tu, Z. & Archer, L. A. Design principles for electrolytes and interfaces for stable lithium-metal batteries. *Nat. Energy* **1**, 16114 (2016).
- Cheng, X.-B. et al. A review of solid electrolyte interphases on lithium metal anode. *Adv. Sci.* **3**, 1500213 (2016).
- Lin, D., Liu, Y. & Cui, Y. Revisiting the lithium metal anode for high-energy batteries. *Nat. Nanotechnol.* **12**, 194–206 (2017).
- Flamme, B. et al. Guidelines to design organic electrolytes for lithium-ion batteries: environmental impact, physicochemical and electrochemical properties. *Green Chem.* **19**, 1828–1849 (2017).
- Aspern, N., Rösenthaller, G.-V., Winter, M. & Cekic-Laskovic, I. Fluorine and lithium: Ideal partners for high-performance rechargeable battery electrolytes. *Angew. Chem. Int. Ed.* **58**, 15978–16000 (2019).
- Jie, Y., Ren, X., Cao, R., Cai, W. & Jiao, S. Advanced liquid electrolytes for rechargeable li metal batteries. *Adv. Funct. Mater.* **30**, 1910777 (2020).
- Fan, X. & Wang, C. High-voltage liquid electrolytes for Li batteries: progress and perspectives. *Chem. Soc. Rev.* **50**, 10486–10566 (2021).
- Hobold, G. M. et al. Moving beyond 99.9% Coulombic efficiency for lithium anodes in liquid electrolytes. *Nat. Energy* **6**, 951–960 (2021).
- Yamada, Y., Wang, J., Ko, S., Watanabe, E. & Yamada, A. Advances and issues in developing salt-concentrated battery electrolytes. *Nat. Energy* **4**, 269–280 (2019).
- Cao, X., Jia, H., Xu, W. & Zhang, J.-G. Review—localized high-concentration electrolytes for lithium batteries. *J. Electrochem. Soc.* **168**, 010522 (2021).
- Ren, X. et al. Enabling high-voltage lithium-metal batteries under practical conditions. *Joule* **3**, 1662–1676 (2019).
- Chen, J. et al. Electrolyte design for Li metal-free Li batteries. *Mater. Today* **39**, 118–126 (2020).
- Holoubek, J. et al. An all-fluorinated ester electrolyte for stable high-voltage li metal batteries capable of ultra-low-temperature operation. *ACS Energy Lett.* **5**, 1438–1447 (2020).

16. Wang, H. et al. Dual-solvent li-ion solvation enables high-performance Li-metal batteries. *Adv. Mater.* **33**, 2008619 (2021).
17. Zhang, H. et al. Electrolyte additives for lithium metal anodes and rechargeable lithium metal batteries: progress and perspectives. *Angew. Chem. Int. Ed.* **57**, 15002–15027 (2018).
18. Yang, Y. et al. Liquefied gas electrolytes for wide-temperature lithium metal batteries. *Energy Environ. Sci.* **13**, 2209–2219 (2020).
19. Weber, R. et al. Long cycle life and dendrite-free lithium morphology in anode-free lithium pouch cells enabled by a dual-salt liquid electrolyte. *Nat. Energy* **4**, 683–689 (2019).
20. Louli, A. J. et al. Diagnosing and correcting anode-free cell failure via electrolyte and morphological analysis. *Nat. Energy* **5**, 693–702 (2020).
21. Yu, Z. et al. Molecular design for electrolyte solvents enabling energy-dense and long-cycling lithium metal batteries. *Nat. Energy* **5**, 526–533 (2020).
22. Amanchukwu, C. V. et al. A new class of ionically conducting fluorinated ether electrolytes with high electrochemical stability. *J. Am. Chem. Soc.* **142**, 7393–7403 (2020).
23. Xue, W. et al. Ultra-high-voltage Ni-rich layered cathodes in practical Li metal batteries enabled by a sulfonamide-based electrolyte. *Nat. Energy* **6**, 495–505 (2021).
24. Holoubek, J. et al. Tailoring electrolyte solvation for Li metal batteries cycled at ultra-low temperature. *Nat. Energy* **6**, 303–313 (2021).
25. Ma, P., Mirmira, P. & Amanchukwu, C. V. Effect of building block connectivity and ion solvation on electrochemical stability and ionic conductivity in novel fluoroether electrolytes. *ACS Cent. Sci.* **7**, 1232–1244 (2021).
26. Xiao, J. et al. Understanding and applying coulombic efficiency in lithium metal batteries. *Nat. Energy* **5**, 561–568 (2020).
27. Chen, Y. et al. Steric effect tuned ion solvation enabling stable cycling of high-voltage lithium metal battery. *J. Am. Chem. Soc.* **143**, 18703–18713 (2021).
28. Pham, T. D. & Lee, K. Simultaneous stabilization of the solid/cathode electrolyte interface in lithium metal batteries by a new weakly solvating electrolyte. *Small* **17**, 2100133 (2021).
29. Xu, R. et al. Designing and demystifying the lithium metal interface toward highly reversible batteries. *Adv. Mater.* **33**, 2105962 (2021).
30. Chen, X. & Zhang, Q. Atomic insights into the fundamental interactions in lithium battery electrolytes. *Acc. Chem. Res.* **53**, 1992–2002 (2020).
31. Kim, S. C. et al. Potentiometric measurement to probe solvation energy and its correlation to lithium battery cyclability. *J. Am. Chem. Soc.* **143**, 10301–10308 (2021).
32. Su, C.-C. et al. Principle in developing novel fluorinated sulfone electrolyte for high voltage lithium-ion batteries. *Energy Environ. Sci.* **14**, 3029–3034 (2021).
33. Wang, H. et al. Efficient lithium metal cycling over a wide range of pressures from an anion-derived solid-electrolyte interphase framework. *ACS Energy Lett.* **6**, 816–825 (2021).
34. Liu, X. et al. Enhanced Li⁺ transport in ionic liquid-based electrolytes aided by fluorinated ethers for highly efficient lithium metal batteries with improved rate capability. *Small Methods* **9**, 2100168 (2021).
35. Halat, D. M. et al. Modifying Li⁺ and anion diffusivities in polyacetal electrolytes: a pulsed-field-gradient nmr study of ion self-diffusion. *Chem. Mater.* **33**, 4915–4926 (2021).
36. Ando, H. et al. Mixture of monoglyme-based solvent and lithium bis(trifluoromethanesulfonyl)amide as electrolyte for lithium ion battery using silicon electrode. *Mater. Chem. Phys.* **225**, 105–110 (2019).
37. Sasaki, Y., Shimazaki, G., Nanbu, N., Takehara, M. & Ue, M. Physical and electrolytic properties of partially fluorinated organic solvents and its application to secondary lithium batteries: Partially fluorinated dialkoxyethanes. *ECS Trans.* **16**, 23–31 (2019).
38. Yue, Z., Dunya, H., Aryal, S., Segre, C. U. & Mandal, B. Synthesis and electrochemical properties of partially fluorinated ether solvents for lithium-sulfur battery electrolytes. *J. Power Sources* **401**, 271–277 (2018).
39. Zhang, Y. & Viswanathan, V. Design rules for selecting fluorinated linear organic solvents for li metal batteries. *J. Phys. Chem. Lett.* **12**, 5821–5828 (2021).
40. Yu, Z. et al. A dynamic, electrolyte-blocking, and single-ion-conductive network for stable lithium-metal anodes. *Joule* **3**, 2761–2776 (2019).
41. Jia, M. et al. Fluorinated bifunctional solid polymer electrolyte synthesized under visible light for stable lithium deposition and dendrite-free all-solid-state batteries. *Adv. Funct. Mater.* **31**, 2101736 (2021).
42. Zou, Y. et al. Interfacial model deciphering high-voltage electrolytes for high energy density, high safety, and fast-charging lithium-ion batteries. *Adv. Mater.* **33**, 2102964 (2021).
43. Aurbach, D., Gofer, Y. & Langzam, J. The correlation between surface chemistry, surface morphology, and cycling efficiency of lithium electrodes in a few polar aprotic systems. *J. Electrochem. Soc.* **136**, 3198–3205 (1989).
44. Adams, B. D., Zheng, J., Ren, X., Xu, W. & Zhang, J.-G. Accurate determination of coulombic efficiency for lithium metal anodes and lithium metal batteries. *Adv. Energy Mater.* **8**, 1702097 (2018).
45. Niu, C. et al. Balancing interfacial reactions to achieve long cycle life in high-energy lithium metal batteries. *Nat. Energy* **6**, 723–732 (2021).
46. Sripad, S., Bills, A. & Viswanathan, V. The iron age of automotive batteries: techno-economic assessment of batteries with lithium metal anodes paired with iron phosphate cathodes. Preprint at *ECSSarXiv* <https://doi.org/10.1149/osf.io/fx4p9> (2021).
47. Eftekhari, A. LiFePO₄/C nanocomposites for lithium-ion batteries. *J. Power Sources* **343**, 395–411 (2017).
48. Nanda, S., Gupta, A. & Manthiram, A. Anode-free full cells: a pathway to high-energy density lithium-metal batteries. *Adv. Energy Mater.* **11**, 2000804 (2021).
49. Park, S. H., Jun, D., Lee, G. H., Lee, S. G. & Lee, Y. J. Toward high-performance anodeless batteries based on controlled lithium metal deposition: a review. *J. Mater. Chem. A* **9**, 14656–14681 (2021).
50. Qian, J. et al. Anode-free rechargeable lithium metal batteries. *Adv. Funct. Mater.* **26**, 7094–7102 (2016).
51. Guo, R. & Gallant, B. M. Li₂O solid electrolyte interphase: probing transport properties at the chemical potential of lithium. *Chem. Mater.* **32**, 5525–5533 (2020).
52. May, R., Fritzsche, K. J., Livitz, D., Denny, S. R. & Marbella, L. E. Rapid interfacial exchange of li ions dictates high coulombic efficiency in li metal anodes. *ACS Energy Lett.* **6**, 1162–1169 (2021).
53. Huang, W., Wang, H., Boyle, D. T., Li, Y. & Cui, Y. Resolving nanoscopic and mesoscopic heterogeneity of fluorinated species in battery solid-electrolyte interphases by cryogenic electron microscopy. *ACS Energy Lett.* **5**, 1128–1135 (2020).
54. Abraham, M. J. et al. GROMACS: High performance molecular simulations through multi-level parallelism from laptops to supercomputers. *SoftwareX* **1–2**, 19–25 (2015).
55. Jorgensen, W. L., Maxwell, D. S. & Tirado-Rives, J. Development and testing of the OPLS all-atom force field on conformational energetics and properties of organic liquids. *J. Am. Chem. Soc.* **118**, 11225–11236 (1996).
56. Dodda, L. S., Cabeza de Vaca, I., Tirado-Rives, J. & Jorgensen, W. L. LigParGen web server: an automatic OPLS-AA parameter generator for organic ligands. *Nucleic Acids Res.* **45**, W331–W336 (2017).
57. Sambasivarao, S. V. & Acevedo, O. Development of OPLS-AA force field parameters for 68 unique ionic liquids. *J. Chem. Theory Comput.* **5**, 1038–1050 (2009).
58. Self, J., Fong, K. D. & Persson, K. A. Transport in superconcentrated LiPF₆ and LiBF₄/propylene carbonate electrolytes. *ACS Energy Lett.* **4**, 2843–2849 (2019).
59. Humphrey, W., Dalke, A. & Schulten, K. VMD: visual molecular dynamics. *J. Mol. Graph.* **14**, 33–38 (1996).
60. Michaud-Agrawal, N., Denning, E. J., Woolf, T. B. & Beckstein, O. MDAAnalysis: a toolkit for the analysis of molecular dynamics simulations. *J. Comput. Chem.* **32**, 2319–2327 (2011).
61. Sinnave, D. The Stejskal-Tanner equation generalized for any gradient shape—an overview of most pulse sequences measuring free diffusion. *Concepts Magn. Reson. Part A* **40A**, 39–65 (2012).
62. Ammann, C., Meier, P. & Merbach, A. A simple multinuclear NMR thermometer. *J. Magn. Reson.* **46**, 319–321 (1982).
63. Spees, W. M., Song, S.-K., Garbow, J. R., Neil, J. J. & Ackerman, J. J. H. Use of ethylene glycol to evaluate gradient performance in gradient-intensive diffusion MR sequences. *Magn. Reson. Med.* **68**, 319–324 (2012).

Acknowledgements

This work is supported by the US Department of Energy, under the Assistant Secretary for Energy Efficiency and Renewable Energy, Office of Vehicle Technologies, the Battery Materials Research Program and Battery500 Consortium. Part of this work was performed at the Stanford Nano Shared Facilities, supported by the National Science Foundation under award no. ECCS-2026822. Z.Y. thanks B. Siegl at Arkema for providing LiFSI. Z.Y. also thanks J. Yang at Stanford University for measuring mass spectrometry and X. Chen at Tsinghua University for discussing the definition of Li⁺ solvates. Z.Z. acknowledges support from Stanford Interdisciplinary Graduate Fellowship. S.T.O. acknowledges support from the Knight Hennessy Scholarship for graduate studies at Stanford University. G.A.K. gratefully acknowledges support from the National Science Foundation Graduate Research Fellowship under grant no. 1650114.

Author contributions

Z.Y., Y.Cui and Z.B. conceived the idea. J.Q., Y.Cui and Z.B. directed the project. Z.Y. designed the logical flow and experiments. Z.Y. performed syntheses, material characterizations, DFT calculations, electrochemical measurements and battery tests. P.E.R., X.K. and J.Q. conducted molecular dynamics simulations and rationales. Z.Z. performed cryo-TEM and cryo-TEM EDS experiments. Z.H. took SEM images and collected viscosity data. H.C. performed DOSY-NMR experiments. S.T.O. collected XPS data. Y.Chen collected ⁷Li- and ¹⁹F-NMR and contributed to key discussion. S.C.K. measured solvation free energies. X.X. carried out ion milling and took part of SEM images. H.W. helped with electrochemical measurements and battery testing. Y.Z. and G.A.K. helped with syntheses. M.S.K. helped with discussion. All authors discussed and analysed the data. Z.Y., S.F.B., J.Q., Y.Cui and Z.B. cowrote and revised the manuscript.

Competing interests

Z.B., Y.Cui. and Z.Y. declare that this work has been filed as US Provisional Patent Application No. 63/283,828. The remaining authors declare no competing interests.

Additional information

Supplementary information The online version contains supplementary material available at <https://doi.org/10.1038/s41560-021-00962-y>.

Correspondence and requests for materials should be addressed to Jian Qin, Yi Cui or Zhenan Bao.

Peer review information *Nature Energy* thanks the anonymous reviewers for their contribution to the peer review of this work.

Reprints and permissions information is available at www.nature.com/reprints.

Publisher's note Springer Nature remains neutral with regard to jurisdictional claims in published maps and institutional affiliations.

© The Author(s), under exclusive licence to Springer Nature Limited 2022